PNAS RESEARCH ARTICLE | EVOLUTION

Primate gut microbiota induce evolutionarily salient changes in mouse neurodevelopment

Alex R. DeCasien[a,b,c,d,1], Jacob E. Aronoff[e,f], Elizabeth K. Mallott[f,g], Sahana Kuthyar[f,h], Sriram Chitta[i], Brian T. Layden[j,k], Maria L. Savo Sardaro[f], Stanton Gray[j], Lawrence E. Williams[i], Emma R. Liechty[j], Hyo M. Lee[b], Won Lee[m,n], James P. Curley[m], Christopher W. Kuzawa[o], and Katherine R. Amato[f,1]

Affiliations are included on p. 10.

Edited by Chet Sherwood, The George Washington University, Washington, DC; received January 4, 2025; accepted October 29, 2025

Multiple primate species, including humans, evolved brains that are exceptionally large relative to their body sizes. These large brains coevolved with metabolic adaptations that enhance cerebral energy supply, including increased circulating glucose levels. While the gut microbiota (GM) is known to influence host metabolism, its potential role in primate brain evolution remains unclear. To investigate this, we inoculated germ-free mice with the GMs of primate species selected to separate the effects of brain size (encephalization) from phylogenetic relatedness: humans (large-brained, Catarrhini), macaques (smaller-brained, Catarrhini), and squirrel monkeys (large-brained, Platyrrhini). We first show that differences in brain gene expression between mice inoculated with human versus macaque GMs resemble those observed between actual human and macaque brains. Comparing the effects of the different primate GMs on mouse brain gene expression further revealed that despite greater evolutionary distance, the GMs from the two larger-brained species (humans and squirrel monkeys) similarly upregulated genes associated with energy production. Notably, human GMs specifically increased the expression of genes involved in oxidative phosphorylation, and these gene expression changes correlated with increased abundances of GM metabolic pathways related to glucose metabolism and gluconeogenesis. Human GMs also downregulated evolutionarily conserved genes implicated in neurodevelopmental disorders such as autism. Although these are findings based on a small sample of primate species and must be interpreted as preliminary, they suggest that species differences in GM composition can influence brain metabolism and raise the possibility that the GM could have played a supporting role in primate encephalization.

gut microbiota | brain evolution | primates

Significance

Compared to other primates, humans have remarkably large brains relative to their body sizes. The resultant high demands for glucose may have been supported by changes in the gut microbiota (GM), which can influence host metabolism. In this study, we tested this idea by inoculating germ-free mice with GMs from three primate species varying in brain size. Brain gene expression differences between mice inoculated with human versus macaque GMs mirrored patterns observed in human versus macaque brains, and human GMs stimulated glucose production and use in the mouse brain. These findings suggest that species differences in GM can influence brain metabolism and raise the possibility that the GM may have supported the energetic demands associated with larger brains in primates.

Human brains contain billions of neurons and are exceptionally large, especially relative to our body sizes (1). These large brains represent a remarkable energetic feat, since the brain is one of the most metabolically costly organs in the human body (1) and the amount of energy available per neuron is constrained by the supply of oxygen and glucose to the brain (2). This suggests that innovations to systemic metabolism must have occurred in the human lineage to facilitate the evolution of large brains (3). Consistent with this, primate species with larger brains also tend to exhibit higher basal metabolic rates (4), daily total energy expenditures (5), fasting blood glucose levels (6), aerobic capacities (i.e., maximum metabolic rates, VO_2 max) (7), and LDH-B:LDH-A expression ratios in the brain (i.e., enzymes that support aerobic vs. anaerobic metabolism) (8, 9). Furthermore, relative to nonhuman primates, humans exhibit more changes in the promoters of genes supporting glucose metabolism (10) and higher expression in the brain of *GLUT1*/*SLC2A1* (encoding the primary glucose transporter) (11) and of genes involved in oxidative phosphorylation, electron transport, and mitochondrial function (12).

In addition to these genomic and physiological alterations, evolutionary changes to the composition of the gut microbiota (GM) could facilitate host metabolic alterations and, therefore, support increased brain sizes (13). The GM regulates host metabolism by extracting energy from the diet and producing various metabolites, including short-chain fatty acids (SCFAs), which serve as energy sources (i.e., substrates for gluconeogenesis and lipogenesis) and also as regulators of colon and liver function (14–17). Glucose metabolism in the brain supports energy-intensive processes like neuronal proliferation, synaptogenesis, myelination, and synaptic plasticity (via aerobic glycolysis) and also ongoing synaptic activity (via oxidative phosphorylation) (18). Furthermore, long-chain FAs, which can be produced by the liver using substrates provided by the GM (19), can cross the blood–brain barrier (20). Pathological alterations to the GM have been linked to both metabolic diseases (e.g., type-2 diabetes, obesity) (14–17, 21–24) and neurodevelopmental conditions (e.g., autism spectrum disorder, ASD; familial dysautonomia) (25, 26), suggesting that the GM is critical for both energy

Author contributions: A.R.D., C.W.K., and K.R.A. designed research; A.R.D., J.E.A., E.K.M., S.K., S.C., B.T.L., M.L.S.S., S.G., L.E.W., E.R.L., H.M.L., W.L., and J.P.C. performed research; E.K.M. contributed new reagents/analytic tools; A.R.D., J.E.A., and K.R.A. analyzed data; and A.R.D., C.W.K., and K.R.A. wrote the paper.

The authors declare no competing interest.

This article is a PNAS Direct Submission.

[1]To whom correspondence may be addressed. Email: alex.decasien@nih.gov or katherine.amato@northwestern.edu.

This article contains supporting information online at https://www.pnas.org/lookup/suppl/doi:10.1073/pnas.2426232122/-/DCSupplemental.

Published January 5, 2026.

balance and typical brain development. Interestingly, metabolic pathways that are differentially expressed in the brains of individuals with ASD are analogous to the microbial pathways that are differentially abundant in the GMs of children with ASD, suggesting that alterations to GM composition may drive coordinated changes in the brain (27).

Comparative studies suggest that GM composition and function differ between primate species (28, 29) and that some of this variation may correlate with relative brain size (30). However, the extent to which GM differences contribute to species differences in metabolism and brain development remains unknown. To address these gaps, we created a model of gut-brain evolution and development by inoculating germ-free mice with the GMs of primate species that vary in encephalization (i.e., brain size relative to body size) and postnatal brain growth rates, including humans (*Homo sapiens*), squirrel monkeys (*Saimiri boliviensis*), and macaques (*Macaca mulatta*) (31). Although humans are more closely related to macaques, the relative brain sizes and postnatal brain growth rates are more similar between humans and squirrel monkeys than between humans and macaques (31), so this model allows us to disassociate the effects of brain size and phylogeny. We previously showed that the GMs of humans and squirrel monkeys similarly induce host energy production via gluconeogenesis in the liver, while the macaque GM stimulates a faster body growth rate and increased deposition of adipose tissue (32). These findings are consistent with a coevolutionary relationship between GM composition, host glucose metabolism, and brain size in primates. Here, we extend our analysis of this unique model system to investigate potential GM effects on the brain (Fig. 1).

Results

Primate GMs Impact Mouse Brain Gene Expression in Ways That Recapitulate Primate Species Differences in Brain Gene Expression. Our dataset consisted of 11,359 detectably

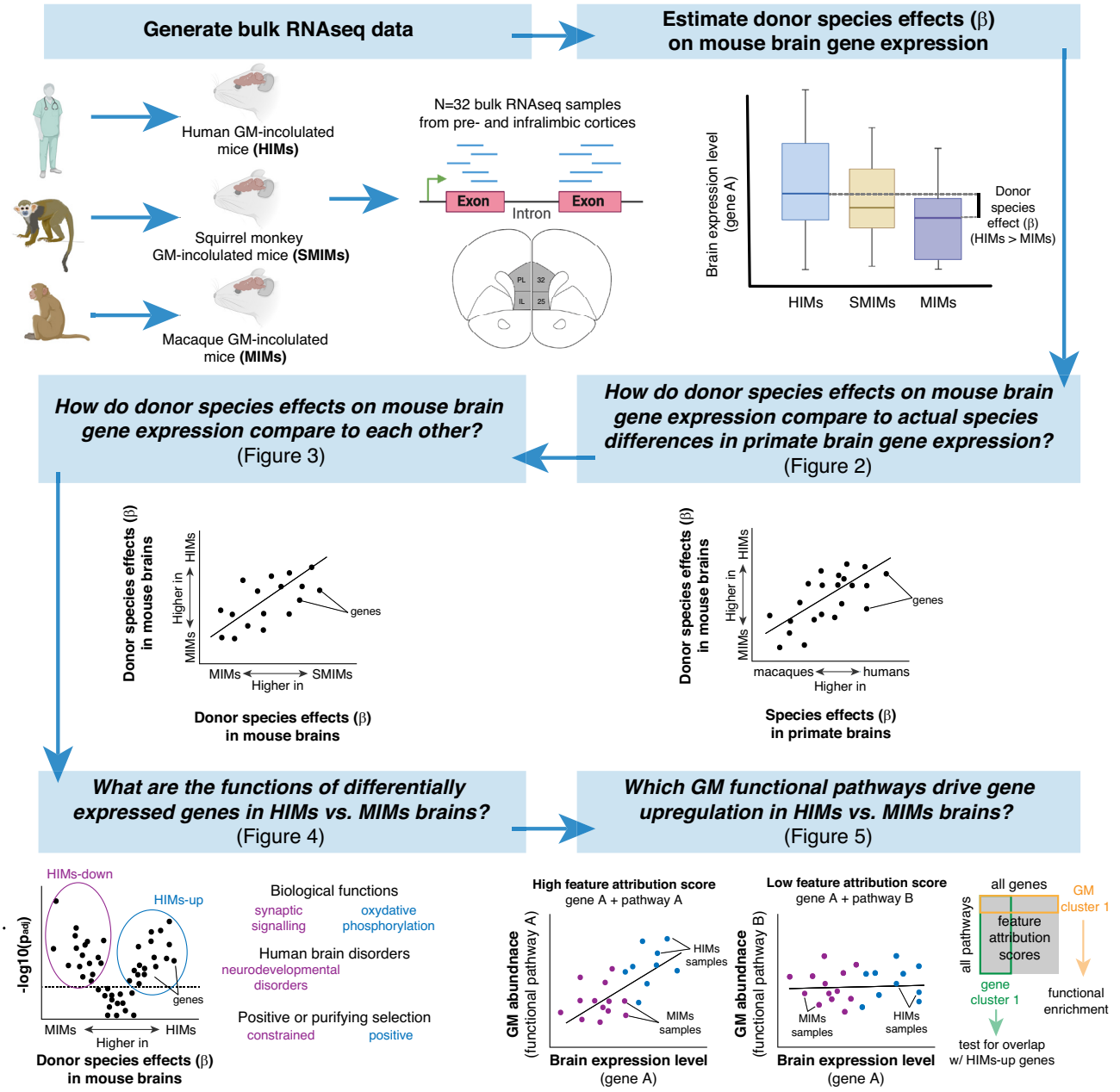

Fig. 1. Diagram of methods, questions, and figures. Infralimbic/prelimbic frontal cortex (IL/PL) of the mouse brain correspond to areas 25 and 32. Created in BioRender. https://BioRender.com/x7lcgmn.

expressed genes (excluding ribosomal genes, see *Methods*) from the infralimbic/prelimbic frontal cortices (FC; corresponding to areas 25 and 32, respectively) of N = 32 mice that were inoculated with the GMs of humans (*Homo sapiens*; N = 12), squirrel monkeys (*Saimiri boliviensis*; N = 8), or macaques (*Macaca mulatta*; N = 12) (Fig. 1 and *SI Appendix*, Table S1 and Dataset S1) (33, 34). We first quantified the drivers of global gene expression variation across all 32 samples by estimating the proportion of expression variance (per gene) explained by the GM donor species (i.e., "gut species") and three PCA-based measures of sample quality (that capture e.g., ribosomal content, mapping rate, and GC content; *Methods*; *SI Appendix*, Fig. S1 and Table S1 and Dataset S1) using linear mixed models (*Methods*). We found that gut species explained an average (median) of 5.65% of expression variation, while technical effects explained relatively less expression variation (medians: PC2 = 5.58%, PC1 = 5.12%, PC4 = 2.81%) (Fig. 2*A* and *SI Appendix*, Table S2 and Dataset S1). This suggests that mice inoculated with the GMs of different primate species exhibit detectable differences in brain gene expression.

To further investigate the impact of gut species on mouse brain gene expression, we modeled normalized expression levels (per gene) as a function of GM donor species and technical variables (*Methods*). We identified hundreds of genes in the mouse FC that were differentially expressed (FDR < 0.2) between human-inoculated mice (HIMs), squirrel monkey-inoculated mice (SMIMs), and macaque-inoculated mice (MIMs) (HIMs vs. MIMs: N = 369 donor

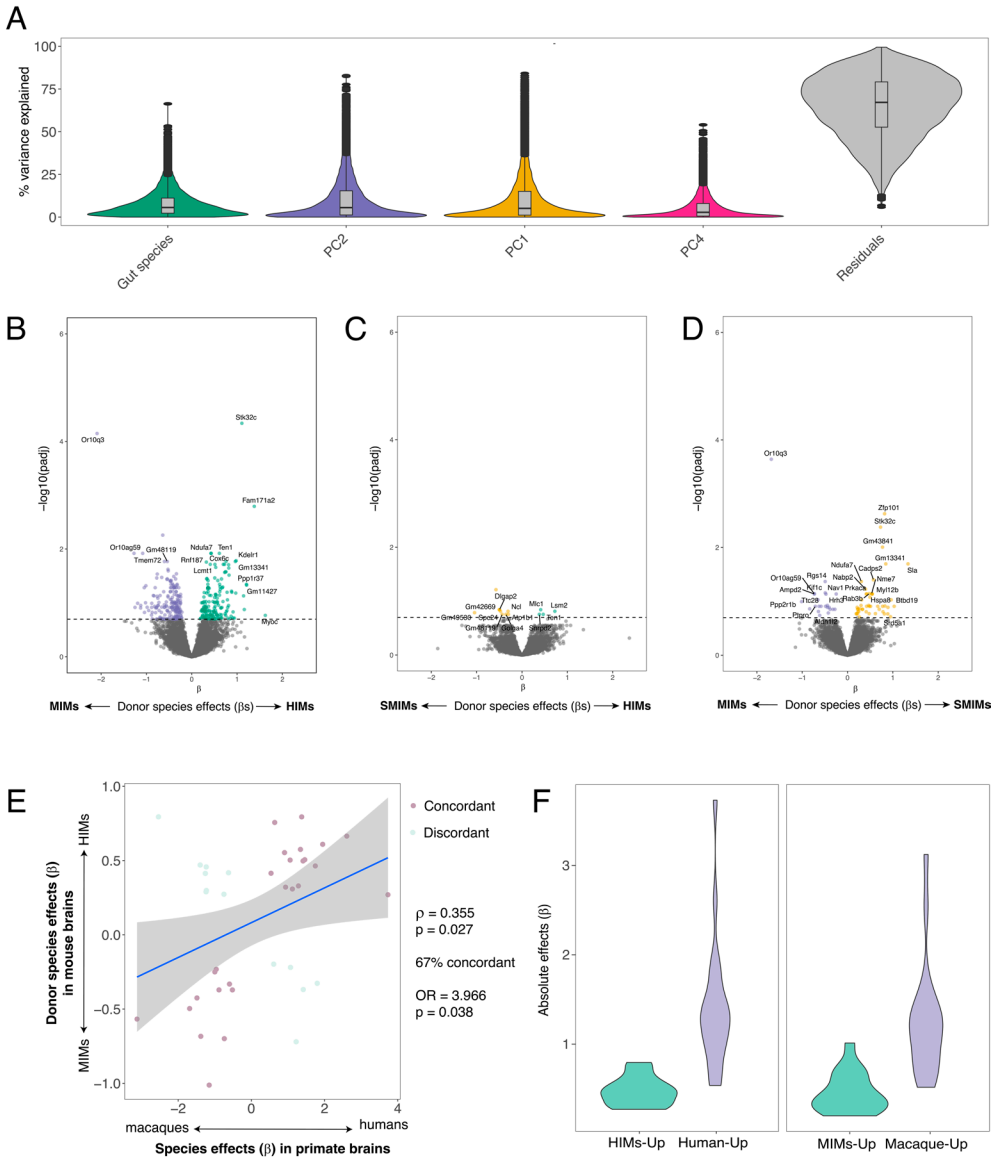

Fig. 2. Donor species effects on mouse brain gene expression. (*A*) Violin plots with overlaid boxplots of variance proportions for each gene and variable from variance partitioning analysis. Boxplots indicate the median (black horizontal line), first and third quartiles (i.e., interquartile range, IQR; *Lower* and *Upper* hinges), and ranges extending from each to 1.5 × IQR beyond each hinge (whiskers). Points represent individual genes that are outliers (i.e., beyond whiskers). (*B*) Differential expression between HIMs and MIMs. Donor species effects (βs = log2 fold change) are on the x-axis and $-\log10(p_{adj})$ values are on the y-axis. Each dot represents one gene, and colors represent expression bias (green = HIMs-upregulated; purple = MIMs-upregulated; gray = no difference). (*C*) Differential expression between HIMs and SMIMs. Donor species effects (βs = log2 fold change) are on the x-axis and $-\log10(p_{adj})$ values are on the y-axis. Each dot represents one gene, and colors represent expression bias (green = HIMs-upregulated; yellow = SMIMs-upregulated; gray = no difference). (*D*) Differential expression between SMIMs and MIMs. Donor species effects (βs = log2 fold change) are on the x-axis and $-\log10(p_{adj})$ values are on the y-axis. Each dot represents one gene, and colors represent expression bias (yellow = SMIMs-upregulated; purple = MIMs-upregulated; gray = no difference). (*E*) Gene expression differences between HIMs and MIMs FCs vs. gene expression differences between human and macaque MFCs. Each point represents 1 gene (N = 39 genes with $p_{adj} < 0.25$ in both analyses; βs = log2 fold change). Colors indicate whether gene expression changes are concordant (pink) or discordant (turquoise) across analyses. The linear regression line and CI are shown. (*F*) Absolute donor species effect sizes (βs = log2 fold change) for genes that are upregulated in both human/HIMs brains or macaque/MIMs brains.

species-related differentially expressed genes (dsDEGs), N = 176 HIMs > MIMs, N = 193 MIMs > HIMs; HIMs vs. SMIMs: N = 13 dsDEGs, N = 4 HIMs > SMIMs, N = 9 SMIMs > HIMs; SMIMs vs. MIMs: N = 70 dsDEGs, N = 23 MIMs > SMIMs, N = 47 SMIMs > MIMs) (Fig. 2 *B–D* and *SI Appendix*, Table S3 and Dataset S1).

We then examined the extent to which the brains of primate GM-inoculated mice mirrored those of their donor species. Put another way, we asked whether the expression differences between HIMs vs. MIMs brains mirrored the differences observed between human vs. macaque brains (we could not include SMIMs/squirrel monkeys due to a lack of data). To test this, we i) estimated gene expression differences between human and macaque medial prefrontal cortices (MFCs; corresponds to areas 24, 32, and 33) using a published dataset (35, 36) (*Methods*; *SI Appendix*, Table S4 and Dataset S1); and ii) compared these differences to those observed between HIMs and MIMs. We found that genes that were up- or downregulated in the FCs of HIMs vs. MIMs also tended to be up- or downregulated in MFCs of humans vs. macaques, respectively (Fig. 2*E* and *SI Appendix*, Fig. S2). Out of N = 8,516 overlapping genes, N = 39 genes were differentially expressed at p_{adj} < 0.25 (*Methods*) in both datasets; 67% of these genes were up- or downregulated in the same direction in both mouse and primate brains; odds ratio [OR] = 3.966, $P = 0.038$), and the effect sizes were positively correlated ($\rho = 0.355$ $P = 0.027$) (*Methods*). Importantly, this pattern was consistent across FDR cutoffs and whether genes were required to pass a given FDR threshold in either dataset or in both datasets (*SI Appendix*, Fig. S2 and Table S5 and Dataset S1; *Methods*). As expected, genes with concordant expression changes across analyses (i.e., those upregulated in both HIMs FCs and human MFCs or those upregulated in both MIMs FCs and macaque MFCs) tended to show larger differences in primate brains compared to mouse brains (Fig. 2*F*) (within each group: *t* test $P < 2.2e{-}16$), suggesting there are additional species-specific mechanisms that contribute to the full magnitude of expression differences between primate brains.

The GMs of Encephalized Species Have Convergent Effects On the Mouse Brain Transcriptome. We next compared the effects of different primate GMs to each other. We predicted that the brain gene expression patterns of mice inoculated with the GMs of more encephalized species (i.e., humans and squirrel monkeys) would be most similar to each other since i) primate GM composition may coevolve with brain size (13); and ii) we previously detected this pattern when examining patterns of fat deposition and liver gene expression in the same mice (32). Our results largely confirm this prediction. Dimensionality reduction suggested that FC samples from MIMs tended to separate from those of HIMs and SMIMs (Fig. 3 *A* and *B* and *SI Appendix*, Fig. S3). Specifically, HIMs and SMIMs centroids were closer together on PC1 and PC2 (Fig. 3*A* and *SI Appendix*, Fig. S3) and exhibited lower pairwise Euclidean distances (Fig. 3*B*). Consistent with this pattern, the largest gene expression differences were observed between HIMs and MIMs, which yielded the greatest number of dsDEGs (Figs. 2 *B–D* and 3*C* and *SI Appendix*, Fig. S3) and the largest effect sizes (Fig. 3*C* and *SI Appendix*, Fig. S3) (mean absolute β's: HIMs vs. MIMs = 0.171, HIMs vs. SMIMs = 0.147, SMIMs vs. MIMs = 0.136; ANOVA $P < 2e{-}16$; Tukey's HSD: all $p_{adj} < 0.001$). Expression differences between HIMs vs. MIMs were similar to those between SMIMs vs. MIMs (Fig. 3*D*), which is consistent with dimensionality reduction (Fig. 3*A* and *SI Appendix*, Fig. S3) and suggests that human and squirrel monkey GMs had similar effects on mouse frontal cortex gene expression (compared to the effects of macaque GMs).

Human GMs Upregulate Genes Linked to Glucose Metabolism and Oxidative Phosphorylation in the Mouse Brain. To illuminate the functions of genes that are differentially expressed in the brains of mice inoculated with the GMs of different donor species, we performed gene ontology enrichment analyses on all sets of dsDEGs (*Methods*; *SI Appendix*, Fig. S4 and Tables S6–S8 and Dataset S1). In line with the aforementioned similarities among the brain transcriptomes of HIMs and SMIMs (vs. MIMs) (Fig. 3 *A–D*), we found that SMIMs vs. MIMs dsDEGs exhibited similar enrichment results as those for HIMs vs. MIMs dsDEGs (including cellular respiration and ATP synthesis) (*SI Appendix*, Tables S6 and S8 and Dataset S1). Accordingly, we focus here on comparisons of HIMs vs. MIMs.

Genes that were upregulated in the brains of HIMs (vs. MIMs) were associated with pathways involved in oxidative phosphorylation, glucose metabolism, and synaptic plasticity ($p_{adj} < 0.05$; Fig. 4*A* and *SI Appendix*, Table S6 and Dataset S1), consistent with previous reports that genes involved in glucose metabolism are upregulated in human brains compared to those of nonhuman primates (10–12) and that oxidative phosphorylation provides metabolic support for synaptic transmission (18). In the opposing direction, genes that were upregulated in MIMs (vs. HIMs) were linked to synaptic signaling and transmembrane transport ($p_{adj} <$ 0.05; Fig. 4*A* and *SI Appendix*, Table S6 and Dataset S1). We delve further into the possible drivers and implications of these enrichments in the following sections, in which we i) explore donor effects on mouse brain cell type proportions, synaptic structures, and genes implicated in human evolution and neurodevelopmental disorders; ii) link regional brain expansion in humans (vs. macaques) to metabolic demands; iii) identify GM functional pathways that drive gene upregulation in HIMs brains.

Primate GMs Do Not Impact Brain Cell Type Proportions. To investigate whether donor group differences in gene expression reflected differences in the proportion of different cell types in the brain, we estimated cell type proportions for each sample using cell type marker genes identified in a meta-analysis of mouse brain cell type markers (37) (*Methods*). We did not find any significant differences after correcting for multiple comparisons (*SI Appendix*, Table S9 and Fig. S5 and Dataset S1), suggesting that the impact of primate GMs on brain gene expression reflects changes in cellular activity, rather than differences in cell type proportions.

Primate GMs Induce Alterations to Synaptic Structures in the Mouse Brain. Our functional enrichment analyses suggested that genes upregulated in HIMs (vs. MIMs) were involved in synaptic plasticity (Fig. 4*A* and *SI Appendix*, Table S6 and Dataset S1). Consistent with this, we also found that *DLG4*—a postsynaptic marker (38) whose expression has been shown to correlate with the number of synapses in the primate brain (39)—was higher in HIMs compared to MIMs (HIMs vs. MIMs: β = 0.39; p_{adj} = 0.07; SMIMs vs. MIMs: β = 0.22; $p_{adj} = 0.37$; HIMs vs. SMIMs: β = 0.17, $p_{adj} = 0.71$) (Fig. 4*B* and *SI Appendix*, Table S3 and Dataset S1). This finding is consistent with previous studies of *DLG4* expression in human vs. nonhuman primate brains (39, 40) cf. (41) and with observations that human brains exhibit more synapses per neuron and larger and longer spines (which have larger postsynaptic densities) (42) compared to those of nonhuman primates (43–46). Increased postsynaptic structures in HIMs vs. MIMs is also consistent with increased energy uptake in HIMs brains, since the highest costs associated with neuronal activity are from excitatory postsynaptic potentials in the dendritic tree and propagation of action potentials along the axon (47). Expression of the presynaptic marker *SYP* (synaptophysin) (48) did not differ

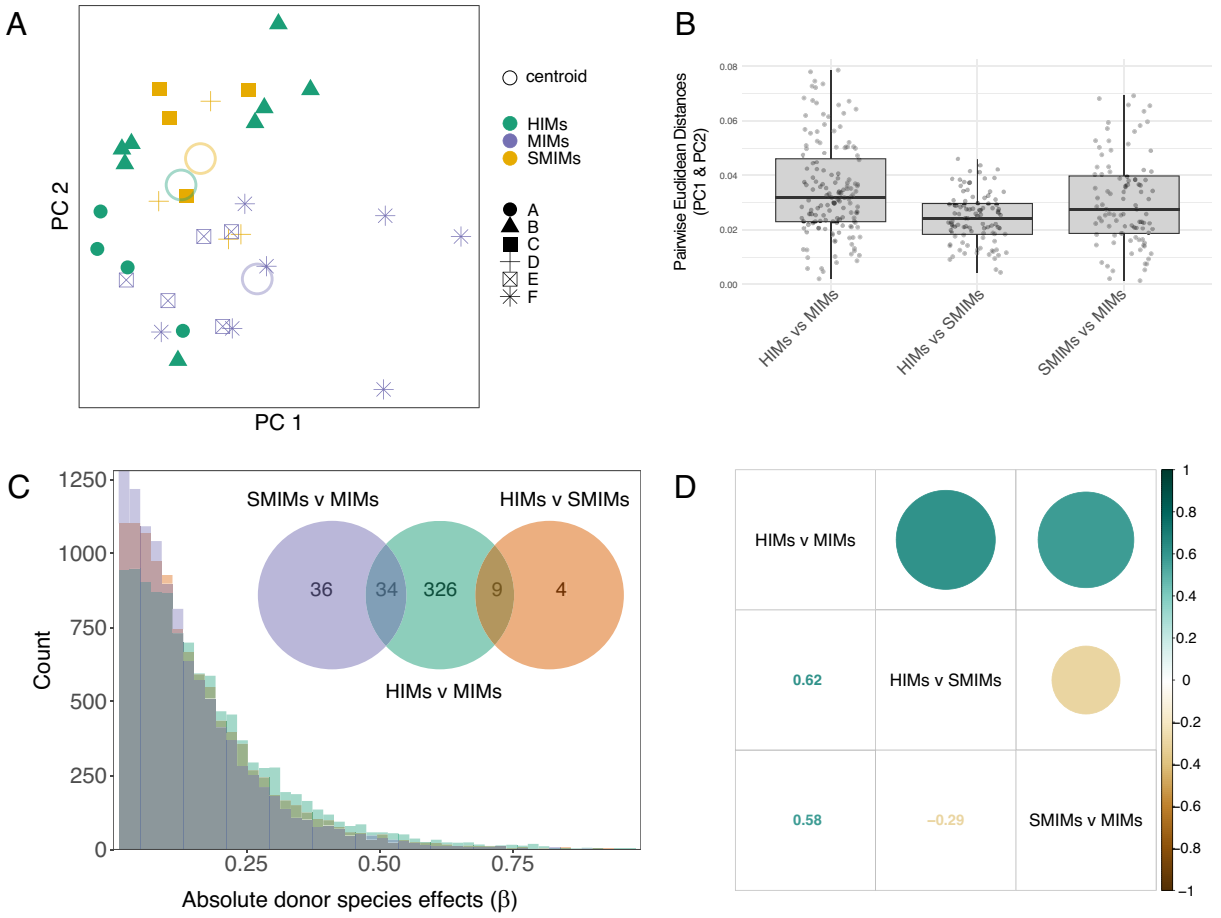

Fig. 3. Primate gut microbiota (GM) effects on mouse frontal cortex gene expression. (*A*) Scatterplot showing principal components (PC1 and PC2) of gene expression data. Each point represents one sample (N = 32). Colors indicate GM donor species and shape indicates batch (see legend). Donor species centroids are shown as open circles (see legend). (*B*) Boxplots showing the pairwise Euclidean distances (between each pair of samples) for PC1 and PC2 (Fig. 3*A*) across donor species. (*C*) Distribution of effect sizes (absolute) across GM donor species comparisons (colors correspond those in the Venn diagram). The inset Venn diagram compares differentially expressed genes across donor species comparisons (FDR < 0.2). (*D*) Correlation plot of effect sizes across GM donor species comparisons. Darker green = more positive correlation, darker orange = negative correlation. Size of circle = strength of correlation. All correlations have $p_{adj} < 0.001$.

between groups (HIMs vs. MIMs: β = 0.12, p_{adj} = 0.52; HIMs vs. SMIMs: β = 0.06, p_{adj} = 0.89; SMIMs vs. MIMs: β = 0.06, p_{adj} = 0.76) (Fig. 4*B* and *SI Appendix*, Table S3 and Dataset S1). This finding was unexpected in light of past work showing correlated expression of *DLG4* and *SYP* across species (39).

Primate GMs Alter the Expression of Genes That Were Subject to Both Positive and Purifying Selection in the Human Lineage. Phenotypic changes can be facilitated by many different (and interconnected) genomic alterations, including (but certainly not limited to) changes in gene regulation, RNA expression level, and protein structure. To investigate whether genes that were differentially expressed in our model system also experienced distinct patterns of selection on their coding regions, we tested for overlap between HIMs vs. MIMs dsDEGs (FDR < 0.2) and protein-coding genes previously identified to have strong signatures of positive or purifying (i.e., constrained) selection in the human lineage (49) (N = 114 overlapping genes) (*Methods*; *SI Appendix*, Table S10 and Dataset S1). We found a nonsignificant association between these lists (Fisher's exact test: OR = 1.814, *P* = 0.131), whereby MIMs-upregulated genes (i.e., those that were upregulated in MIMs vs. HIMs brains) showed stronger overlap with evolutionarily constrained genes than with those subject to positive selection in the human lineage (MIMs-upregulated genes: total N = 50; positive: N = 17, 34%; purifying: N = 33, 66%). Our findings that MIMs-upregulated genes tend to be both conserved and involved in synaptic transmission (Fig. 4*A* and *SI Appendix*, Table S6 and Dataset S1) are in line with previous work showing that genes associated with synapses tend to be conserved in the human lineage (49). Compared to MIMs-upregulated genes, HIMs-upregulated genes were more likely to exhibit signatures of positive selection (HIMs-upregulated: total N = 64; positive: N = 31, 48%; purifying: N = 33, 52%). This may reflect, in part, coordinated changes in protein coding regions and brain gene expression levels during human evolution, and is consistent with recent evidence of parallel transcriptomic and coding sequence divergence across species (50, 51).

Human GMs Downregulate Genes Implicated in Neurodevelopmental Disorders. Given that primate GMs induce changes to the expression of genes involved in brain development and synapses (Fig. 4*A* and *SI Appendix*, Fig. S4 and Tables S6–S8 and Dataset S1), we tested whether dsDEGs were associated with human brain disorders (*SI Appendix*, Tables S11–S13 and Dataset S1). We found that genes upregulated in MIMs (vs. HIMs) brains were enriched for genes implicated in human neurodevelopmental and psychiatric conditions, including intellectual disability, ASD, ADHD, bipolar disorder, and schizophrenia (all $p_{adj} < 0.05$) (Fig. 4*C* and *SI Appendix*, Table S11 and Dataset S1). This is consistent with a previous report of a gene coexpression module that is both down-regulated in humans (vs. chimpanzees and macaques) and enriched for genes implicated in ASD, ADHD, bipolar disorder, and schizophrenia (52). These findings are also in line with our finding that MIMs-upregulated genes may be

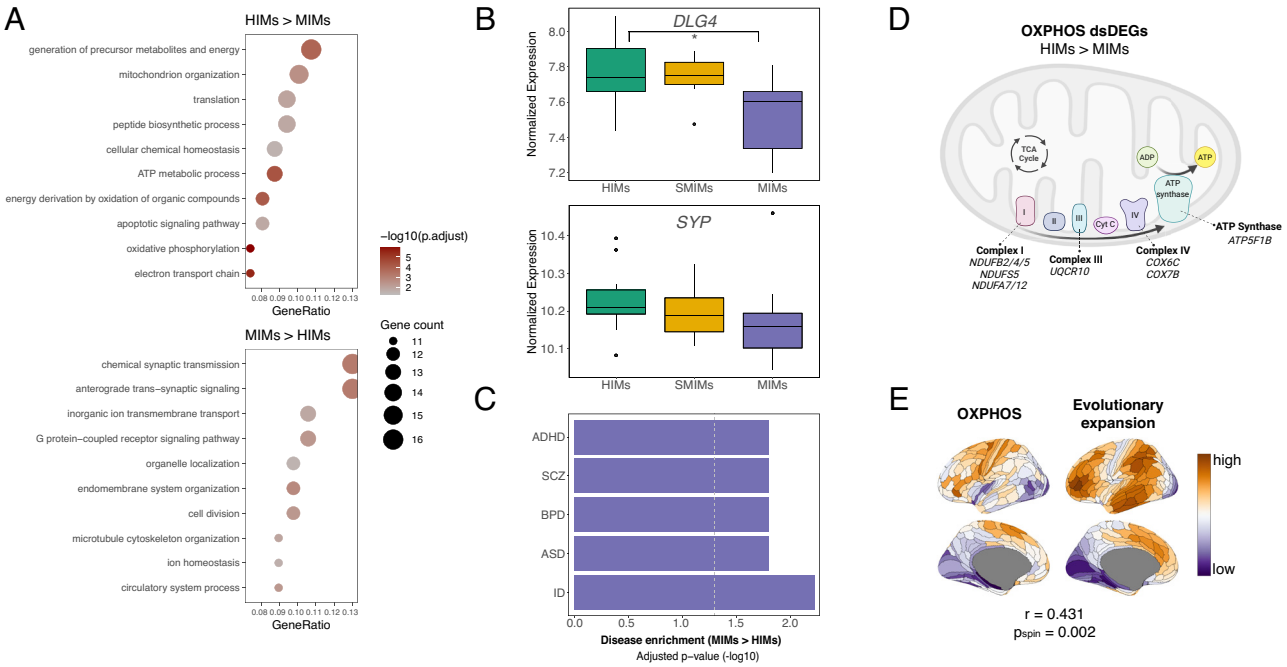

Fig. 4. Effects of human vs. macaque GMs on mouse brain transcriptomes. (*A*) Dot plot depicting GO enrichment results for genes that are upregulated in either HIMs (vs. MIMs; *Top*) or MIMs (vs. HIMs; *Bottom*). Gene ratios are shown on the x-axis for each of the top 10 enriched processes. Dot size reflects gene count and dot color reflects the –log10(*P*-value) of the enrichment (see legend). (*B*) Normalized expression levels for synapse marker genes *DLG4* (*Top*) and *SYP* (*Bottom*). Asterisks indicate FDR < 0.2. (*C*) Bar chart depicting adjusted *P*-values (–log10) of disease enrichments (KS tests) for genes upregulated in MIMs (vs. HIMs). The vertical dotted line corresponds to p_{adj} = 0.05. ID = intellectual disability, SCZ = schizophrenia, ASD = autism spectrum disorders, ADHD = attention deficit hyperactivity disorder, BPD = bipolar disorder. (*D*) Visualization of the HIMs upregulated genes that are involved in oxidative phosphorylation (OXPHOS). Created in BioRender. https://BioRender.com/oposg4c. (*E*) Brain maps showing mean OXPHOS gene expression (*Left*) and evolutionary expansion (in humans vs. macaques) (*Right*). Orange = high expression or expansion; purple = low expression or expansion (see legend). These maps exhibit significant spatial overlap (r and p_{spin} values are shown).

more likely to be subject to purifying selection, since the latter are enriched for neurodevelopmental disorder risk genes (even more than positively selected genes) (49). Furthermore, both MIMs-upregulated genes (in this study; *SI Appendix*, Table S3 and Dataset S1) and evolutionarily constrained genes [from (49)] are enriched for synapses (*SI Appendix*, Table S6 and Dataset S1) (49), and there is a tendency for synaptic genes to be implicated in neurodevelopmental disorders (53, 54).

Human Brain Expansion Overlaps With Brain Areas Showing Increased Oxidative Phosphorylation. Multiple genes involved in oxidative phosphorylation (OXPHOS) were upregulated in HIMs (vs. MIMs) brains (Fig. 4 *A* and *D* and *SI Appendix*, Tables S3 and S6 and Dataset S1). We hypothesized that this may reflect increased OXPHOS demands in specific brain areas, namely, those that underwent evolutionary expansion in the human lineage. To test whether brain areas that are expanded in humans (compared to macaques) (55) also exhibit elevated OXPHOS activity, we performed a spin test of the spatial correlation between i) a map of human (vs. macaque) cortical expansion (55) (Fig. 4*E*); and ii) a map of mean OXPHOS gene expression (56) (Fig. 4*E*) (*Methods*). These maps significantly overlapped (r = 0.431, p_{spin} = 0.002) (Fig. 4*E*), suggesting that increased energy demands in the human brain are linked to the expansion of specific cortical regions.

The Effect of Human GMs on Mouse Brain Transcriptomes Is Modulated By Microbes Involved in Glucose Metabolism. Thus far, we have shown that the GMs of the two phylogenetically distantly related, but encephalized, primate species (including humans and squirrel monkeys) have convergent effects on the mouse brain transcriptome and that these alterations may reflect increased energy generation. To identify specific GM functional pathways that may drive these patterns, we used the neural network framework MiMeNet (57) to i) identify correlated changes in GM functional pathways and gene expression levels in the mouse brain; and ii) link specific GM functional pathways to patterns of differential gene expression between HIMs vs. MIMs brains (*Methods*; Fig. 1) (32–34, 58).

We applied this method to all samples and found N = 1,214 genes and N = 346 GM functional pathways with significant feature attribution scores (*Methods*). These were clustered into 7 gene expression modules (GEMs) and 8 functional pathway modules (FPMs), respectively, based on their feature attribution scores (Fig. 5 and *SI Appendix*, Tables S14 and S15 and Dataset S1). We then tested each GEM for overlap with genes that are upregulated in HIMs vs. MIMs (FDR < 0.2), and identified four HIMs-upregulated GEMs (GEMs 0, 1, 3, and 6; ORs > 1 and p_{adj} < 0.05) (Fig. 5 and *SI Appendix*, Table S16 and Dataset S1). To determine which FPMs were most associated with these four HIMs-upregulated GEMs, we i) averaged the feature attribution scores within each FPM × GEM combination (7 GEMs × 8 FPMs = 56 combinations); ii) calculated the mean feature attribution score across the four HIMs-upregulated GEMs for each FPM; and iii) ranked all FPMs by these mean scores (Fig. 5). This analysis allowed us to identify the GM functional pathways that most strongly influence the expression of genes upregulated in HIMs brains and to prioritize pathways that may mediate gut–brain interactions underlying these expression differences. This analysis revealed that FPMs 1 and 4 had the largest positive effects on HIMs-upregulated genes and included pathways related to glucose degradation (FPMs 1 and 4) and gluconeogenesis (FPM 1) (Fig. 5 and *SI Appendix*, Tables S14 and S15 and Dataset S1). These results suggest that differences in gene expression between HIMs and MIMs brains may be mediated

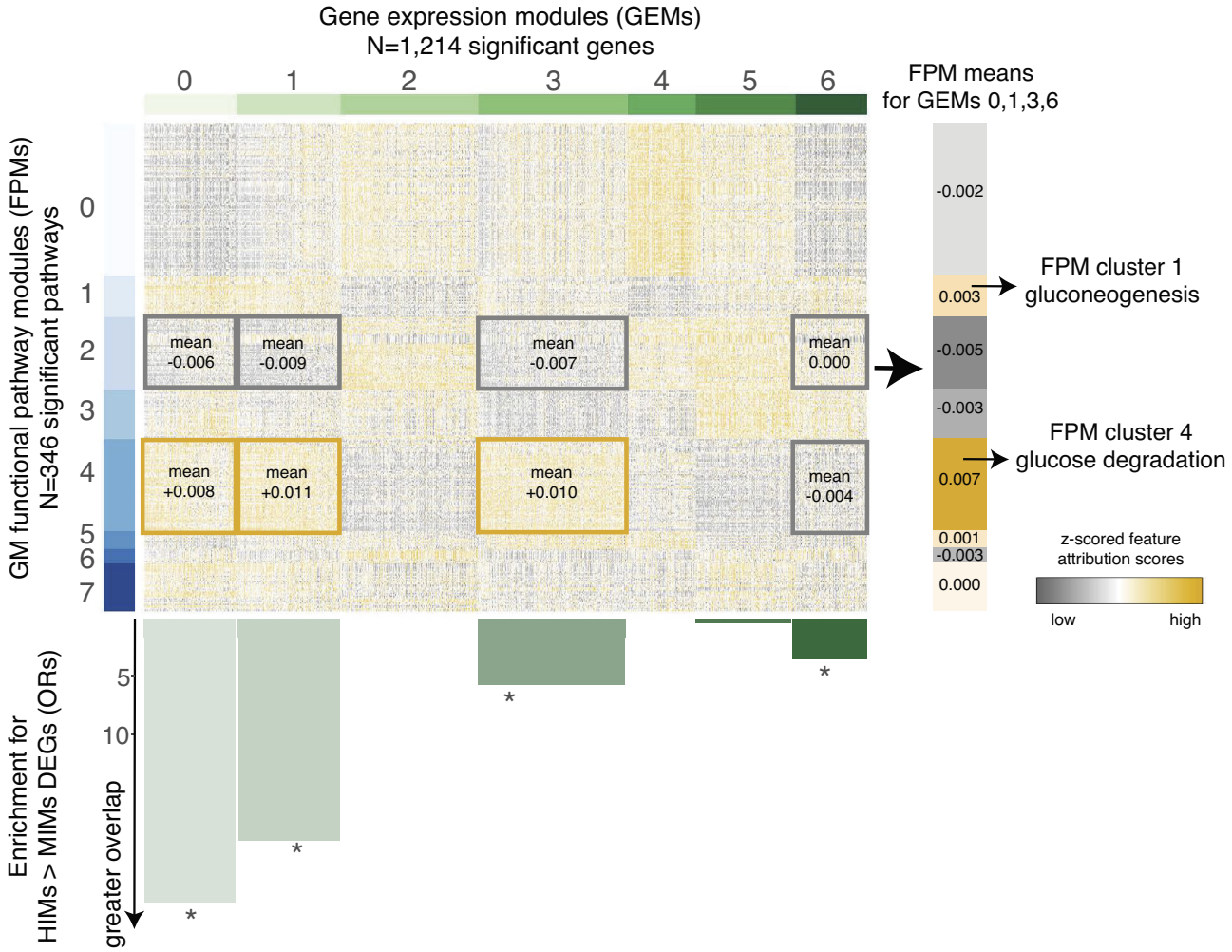

Fig. 5. Linking HIMs-upregulated brain gene expression to specific GM functional pathways. The matrix shows the feature attribution scores for N = 1,214 genes (separated into N = 7 gene expression modules, GEMs; green) and N = 346 GM functional pathways (separated into N = 8 functional pathway modules, FPMs; blue). These values were derived from the MimeNet analysis (*Methods*). Darker yellow scores = stronger positive effect of GM functional pathway abundance on gene expression; darker gray scores = stronger negative effect of GM functional pathway abundance on gene expression (see legend). The bar plot below the matrix shows the enrichment scores (ORs = odds ratios) for genes that are upregulated in HIMs vs. MIMs (FDR < 0.01) in each GEM. GEMS 0, 1, 3, and 6 are significantly enriched for HIMs-upregulated genes (indicated with asterisks). The panel to the right of the matrix shows the mean feature attribution score for each FPM across the three HIMs-upregulated GEMS (0, 1, 3, 6). We note that FPMs 1 and 4 have the highest mean feature attribution scores with HIMs-upregulated GEMS and that these FPMs include gluconeogenesis and glucose metabolism pathways, respectively.

by increased abundance of gut microbes involved in glucose metabolism and gluconeogenesis in HIMs.

Discussion

Our findings suggest that GM from different primate species influence brain gene expression in germ-free mice and that these differences may recapitulate evolutionary changes observed across primate brains. GMs from more encephalized species—humans and squirrel monkeys—induced similar transcriptional changes in the mouse frontal cortex, including upregulation of genes involved in energy generation. These effects were observed despite the greater phylogenetic distance between humans and squirrel monkeys (an American monkey estimated to share a last common ancestor with humans 47 Mya) compared to humans and macaques (an African monkey sharing a last common ancestor with humans 32 Mya). The microbial effects we observed parallel known gene expression differences between human and macaque brains and correspond to cortical regions that expanded during human evolution. This raises the possibility that GM composition may have supported aspects of brain energy demands associated with encephalization, although alternative explanations, such as species-specific traits unrelated to brain size, cannot be excluded.

We also found that human GMs are associated with downregulation of evolutionarily conserved genes implicated in neurodevelopmental disorders. These genes are typically intolerant to mutation, highlighting a potential role for the microbiome in modulating genes essential for healthy brain function. While many genomic and physiological adaptations have evolved to support the high energetic cost of the human brain—such as increased basal metabolic rates and glucose transporter expression—our previous work shows that GMs from encephalized species also promote gluconeogenesis in the liver (32). Here, we extend those findings to the brain, where microbial functional pathways related to glucose degradation and gluconeogenesis are more abundant in human GMs and associated with increased expression of genes linked to synaptic plasticity and oxidative phosphorylation in the mouse brain.

We acknowledge that including more species (including e.g., a less-encephalized Platyrrhine species) would provide a more complete evolutionary contrast to test the hypothesis that GM

composition correlates with encephalization. However, logistical and funding constraints limited the number of species and treatments we were able to include in this initial experiment. We hope that the striking findings we uncovered will motivate follow-up studies incorporating additional nonhuman primate species. In future tests with expanded species sample sizes, it will be important to take care when selecting species to target differences in encephalization specifically. For instance, it is notable that most less-encephalized Platyrrhines that are commonly housed in research centers give birth to multiple offspring per litter, which would introduce life history and energetic differences that could confound encephalization-related signals. Although our findings using only three species must necessarily be viewed as preliminary, our results provide a valuable contribution to understanding the physiological correlates of encephalization in primates. These findings are consistent with the hypothesis that gut microbial differences could have supported metabolic and other demands associated with primate and human encephalization, but additional studies will be needed to test this idea directly.

Methods

Data Collection.

Mice. Germ-free mice were inoculated with the GM samples derived from three primate species (humans, *Homo sapiens*; squirrel monkeys, *Saimiri*; macaques, *Macaca*). The original donors included adults (across all species), juveniles (nonhuman primates), and infants (humans). Fecal samples were collected from humans, captive macaques, and squirrel monkeys as described by Mallott et al. (32) and stored at –80 °C in 1X PBS with 15% glycerol until use.

To inoculate the mice, glycerol stocks from stool samples from five individuals of each species were homogenized, pooled, and diluted with sterile PBS to create a gavage solution. We chose which samples to pool pseudorandomly after checking for clear outliers in GM composition via 16S rRNA gene amplicon sequencing. Two pools were generated for each donor species. Each gavage solution was used to inoculate ten pair-housed weanling germ-free C57BL/6NTac mice via oral gavage (n = 20 mice per donor species). Gnotobiotic mice were maintained in a flexible-film isolator for the 60-d duration of the study in conditions described by Mallott et al. (32). Gavage was repeated weekly to ensure maintenance of the donor GM.

Data and samples, including fecal samples, were collected from the mice throughout the duration of the study as described by Mallott et al. (32). At the end of the 60-d experiment, mice were euthanized in accordance with the NU IACUC, and samples of select organs, including the brain, were flash frozen. The animal care and use program at Northwestern University is accredited by AAALAC International and all animal work was approved by the NU IACUC #IS00006555.

Dissections. Brains were stored at −80Â °C until dissection. Samples of the infralimbic/prelimbic region of the medial frontal cortex (FC) [areas 25 and 32, respectively (59)] were collected using a Harris Micro-Punch with reference to the coronal plane from the Mouse Brain Atlas (60) and the Allen Brain Atlas (61). Due to specimen damage in transit, we were unable to dissect some samples. Our final dataset included samples from 12 human-inoculated mice, 8 squirrel-monkey-inoculated mice, and 12 macaque-inoculated mice.

RNA quantification. Total RNA was isolated using the MagMAX™ mirVana™ Total RNA Isolation Kit. This was followed by 3′ RNA-based library prep and Tag-based RNA-seq (TagSeq) on the NovaSeq 2000 SR100 (33). Cutadapt (62) was used for adaptor trimming and PCR duplicates were removed prior to further analysis. Reads were mapped to the *Mus musculus* Ensembl transcriptome using Bowtie2 (33, 34, 63).

Statistical Analysis. All statistical analyses were performed using R v4.0.0 (64).

Filtering and normalization. Prior to further RNA-seq data analysis, we filtered out genes that were very lowly or not detectably expressed in our samples. Specifically, we removed genes with an average CPM less than 10 in all donor species × batch groups, resulting in 11,450 genes across 32 samples. We calculated normalization factors using the TMM method (*calcNormFactors* in the R package *edgeR*) (65) and normalized the read count matrix (*voomWithQualityWeights* function in the R package *limma*) (66).

Sample quality. For each sample, we obtained the following five sample quality measures: mapping rates, number of reads, percent ribosomal content (the proportion of all reads from ribosomal protein-coding RNAs, i.e., *Rpl/s* genes), percent duplicates, and mean GC content. Many of these measures were correlated (*SI Appendix*, Fig. S1), so we used a PCA approach to derive measures of sample quality. In particular, we 1) ran a PCA on the correlation matrix of normalized expression (*cor* and *prcomp* functions in the R package *stats*); 2) extracted 10 PCs that explained >=1% of the variance (*SI Appendix*, Fig. S1); and 3) tested for an association between each of these PCs with the sample quality measures (using ANOVA) (*SI Appendix*, Fig. S1). *P* values were adjusted across all variable × PC combinations using Bonferroni (*p.adjust* function in the R package *stats*). We found that PC1 captured % ribosomal content ($F = 24.9$; $p_{adj} < 0.05$), PC2 captured GC content ($F = 28.7$; $p_{adj} < 0.05$), and mapping rate ($F = 16.4$; $p_{adj} < 0.05$), and PC4 captured mapping rate ($F = 14.7$; $p_{adj} < 0.05$) (*SI Appendix*, Fig. S1). Accordingly, these PCs were used as measures of sample quality in downstream analyses.

We then repeated *voom* normalization (as above) after removing ribosomal protein-coding RNAs (i.e., *Rpl/s* genes) (11,359 expressed genes remained) using the *voomWithQualityWeights* function in the R package *limma* and previously estimated normalization factors.

Variance partitioning. We performed variance partitioning on the normalized, filtered expression matrix using the *fitExtractVarPartModel* and *plotVarPart* functions in the R package *variancePartition* (67). This function allowed us to fit a linear mixed model to estimate contribution of multiple sources of variation while simultaneously correcting for all other variables. We modeled the expression of each gene as a function of donor species and the three PCs (PC1, PC2, PC4) that capture sample quality. Categorical terms were modeled as random effects, as recommended by the package's creator (68).

Differential expression. For each gene, normalized expression was modeled as a function of donor species × batch (2 batches per species = 2 × 3 = 6 factor levels) and the three PCs (PC1, PC2, PC4) that capture sample quality using linear models implemented with the *lmFit* function in the R package *limma* (66). Contrasts were created to extract differences between all pairs of donor species (i.e., human vs. macaque, human vs. squirrel monkey, and squirrel monkey vs. macaque) using the *contrasts.fit* function in the R package limma (66). The outputs of these models were then used for empirical Bayes moderation of the SE toward a global value, implemented with the function *eBayes* in the R package *limma* (66). *P* values were adjusted with the Benjamini & Hochberg method (69) (*p.adjust* function in the R package *stats*). Due to the limited sample size of our study and the exploratory nature of the analysis, we applied a relaxed significance threshold of FDR < 0.2 to identify differentially expressed genes. This threshold i) balances sensitivity and specificity; ii) is consistent with previous studies in similar contexts (70–72); and iii) facilitates the identification of gene sets for downstream pathway analysis and hypothesis generation. We interpret these results cautiously, emphasizing patterns at the pathway level rather than individual genes alone.

We also estimated *P*-values using a permutation-based approach. Across 1,000 iterations, we shuffled the donor species labels and re-estimated the t-statistics using differential expression modeling (see above). The permutation *P*-value for each gene was estimated as the proportion of t-statistics (absolute value) that were larger than the observed t-statistic (absolute value). These *P*-values were very similar to the original *P*-values (*SI Appendix*, Fig. S3 *D-E*). *P* values were adjusted with the Benjamini & Hochberg method (69) (*p.adjust* function in the R package *stats*).

Comparison to primate species differences in brain gene expression. We downloaded human and rhesus macaque medial prefrontal cortex (MFC) gene expression data from psychENCODE (35). These data were generated by the same group (35) and were mapped using the *XSAnno* pipeline, which was developed by this group to generate annotation of human-macaque orthologs (35). We removed genes with an average CPM less than 5 in both species, resulting in 10,969 genes. We normalized the read count matrix using the functions *calcNormFactors* in the R package *edgeR* (65) and *voom* in the R package *limma* (66). For each gene, normalized expression was modeled as a function of species, age group (fetal vs. nonfetal), age, sex, RIN, sequencing platform (2 levels), and RNA extraction method (2 levels) using linear models implemented with the *lmFit* function in the R package *limma* (66). Contrasts were created to extract differences between humans and macaques using the *contrasts.fit* function in the R package *limma* (66). The outputs of these models were then used for empirical

Bayes moderation of the SE toward a global value, implemented with the function *eBayes* in the R package *limma* (66). *P* values were adjusted with the Benjamini & Hochberg method (69) (*p.adjust* function in the R package *stats*).

Mus musculus Ensembl gene IDs from our primary analysis were converted to one-to-one orthologous human Ensembl gene IDs using R package *biomaRt* (73), resulting in 8,516 genes overlapping between the datasets. We then estimated Spearman's rank order correlations between i) the species effects in the primate dataset (human vs. macaque MFC expression); and ii) the donor species effects in our dataset (HIMs vs. MIMs FC expression). These correlations were performed for genes that passed various FDR cutoffs in either analysis or in both analyses (FDR from 0.01 to 1 in increments of 0.1). We also estimated odds ratios from Fisher's exact tests (on contingency tables based on estimated positive/negative effects in the human vs. macaque and HIMs vs. MIMs analyses) for genes that passed these FDR cutoffs. As an example, we show the overlap between datasets at FDR = 0.25 (Fig. 2*E*) because this was the minimum FDR value that produced significant correlations and ORs while including > 10 genes (when genes were required to pass this threshold in both analyses).

Dimensionality reduction. To visualize interspecies variation in gene expression independent of batch effects, we first adjust for latent covariates (PC1, PC2, and PC4) (*removeBatchEffect* function in the R package *limma*). Principal component analysis (PCA) was then performed on the correlation matrix of the batch-corrected expression data (*cor* and *prcomp* functions in the R package *stats*). Sample scores on the first two principal components (PC1 and PC2) were plotted by species and batch to assess clustering and species separation. For each species, the centroid was calculated as the mean PC1 and PC2 coordinates of its samples and overlaid as a large semitransparent point to aid visual comparison of interspecies differences (Fig. 3*A*). To quantify transcriptomic distances between species, we calculated Euclidean distances between all sample pairs across PC1 and PC2. For each pair of species, we computed the pairwise distance between all samples from each species. These between-species distances were visualized as boxplots (Fig. 3*B*). We also show the results of additional dimensionality reduction approaches, including tSNE (*Rtsne* function in the R package *Rtsne*) (74) and UMAP (*umap* function in the R package *umap*) (75) (*SI Appendix*, Fig. S3 *A–C*).

Functional enrichment analysis. Gene ontology (GO) enrichment analyses were performed using the *enrichGO* function in the R package *clusterprofiler* (76). *Mus musculus* Ensembl IDs were matched to human Ensembl IDs using one-to-one orthologues from the R package *bioMart* (73). These IDs were converted to Entrez gene IDs using the *bitr* function in the R package *clusterprofiler* (76) (OrgDb = org.Hs.eg.db). Enrichment analyses were conducted on upregulated and downregulated genes separately (within each donor contrast), with each set of genes defined as those that were significantly differentially expressed (FDR < 0.2). For each test, background genes represented all expressed genes. *P* values were adjusted using the Benjamini–Hochberg method (69) and pathways with $p_{adj} < 0.05$ were considered significant.

Cell type enrichment analysis. We estimated cell type proportions for each sample using cell type markers from the R package BRETIGEA (BRain cEll Type specIfic Gene Expression Analysis) (37). In this package, the "markers_df_mouse_brain" data frame contains the top 1000 marker genes (ranked by specificity) from each of the six major brain cell types (i.e., astrocytes, endothelial cells, microglia, neurons, oligodendrocytes, and OPCs), which were estimated from their meta-analysis of brain cell gene expression data from mice (*Mus musculus*). We used these markers as input for the *findCells* function to estimate surrogate proportion variables (i.e., cell type proportions) for each sample. Within each cell type, we tested for group differences in cell type proportions using ANOVA tests and Tukey's HSD (*aov* and *TukeyHSD* functions in the R package *stats*).

Analysis of selective pressures. We collected ω values (i.e., d*N*/d*S* values, z-scored and corrected for GC content) and gene names from ref. 49. These were merged with our dataset using external gene names from the R package *biomaRt* (73). We then applied a Fisher's exact test to N = 114 genes that were differentially expressed between HIMs and MIMs (FDR < 0.2) and exhibited extreme ω values (absolute values > 0.49 [which is the median absolute deviation]; low values = purifying selection; high values = positive selection) in the *Homo sapiens* lineage.

Disease gene set enrichment analysis (GSEA). Gene set enrichment analyses for disease ontology (DO) terms were performed using human risk genes downloaded from the DISEASES resource, which integrates the results of text mining and manually curated disease-gene associations, cancer mutation data, and genome-wide association studies from existing databases (77). *Mus musculus* Ensembl IDs were linked to human diseases from this database using one-to-one human orthologues (and their associated genes) from the R package *bioMart* (73). Diseases with at least 10 associated genes were retained for further analysis. Genes were ranked according to their standardized β's for each donor species comparison (HIMs vs. MIMs, HIMs vs. SMIMs, and SMIMs vs. MIMs). For each disease in the final dataset (N = 1,036), we used two-sample Kolmogorov–Smirnov (KS) tests to compare the cumulative distribution functions of the standardized β's of genes associated with the disease to those associated with every other disease in the dataset. We tested two alternative hypotheses, namely that the cumulative distribution function for the target set was either less than or greater than that of the background set. *P* values were adjusted using the Benjamini–Hochberg method (69).

Comparing human brain expansion and OXPHOS maps. We sought to assess the association between regional distributions of oxidative phosphorylation and evolutionary expansion in the cortex. To that end, we obtained the mean regional expression map of N = 49 curated genes tagging for oxidative phosphorylation derived from Allen Human Brain Atlas postmortem adult human brain (56) and the regional patterning of evolutionary hierarchy indexed by macaque-to-human cortical areal expansion (3). These data were mapped onto 360 cortical parcels in the multimodally derived Human Connectome Project regional parcellation (78) (Fig. 4*E*). We then computed the cortex-wide Pearson correlation between these cortical maps. The statistical significance was determined by a spin test (79), in which the correlation between the two cortical maps was compared to the null distribution of 10,000 spatial correlations from random spin-based spatial permutations of one of the cortical maps, yielding an empirical *P* value (p_{spin}) (Fig. 4*E*).

Correlating mouse brain gene expression and microbial pathways. We used MiMeNet (57)–which applies a neural network framework for modeling microbe-expression relationships–to identify correlated changes in the proportions of GM functional pathways and gene expression levels in the mouse brain. This was performed for N = 28 samples for which both brain gene expression (33, 34) and GM functional pathways were available (32, 58, 80). Normalized abundances of GM functional pathways for each sample were estimated using shotgun sequencing following metagenomic library preparation as described by Mallott et al. (32, 58, 80). Briefly, DNA was extracted from mouse fecal samples collected at the final time point using the Qiagen DNeasy PowerSoil Kit with slight modifications. Libraries were constructed using a NuGen Celero with Enzymatic Fragmentation kit using the manufacturers protocol, pooled, size-selected to 400 to 600 bp and sequenced on the Illumina NovaSeq SP 2x150 platform at the Genome Research Core at the University of Illinois Chicago. Raw sequences were quality-filtered and trimmed using KneadData (http://huttenhower.sph.harvard.edu/kneaddata). The HUMAnN2 processing pipeline was used for taxonomic and functional profiling (81). The resulting gene family tables were regrouped into KEGG orthogroups, normalized to copies per million, and split into stratified and unstratified tables. Pathway abundance tables were split into stratified and unstratified tables.

We provided paired normalized brain gene expression levels (see above) and normalized GM functional pathway abundances to the MiMeNet_train.py function (from github) with the following network hyperparameters: "num_layer" = 1, "lr" = 0.001, "layer_nodes" = 512, "l2" = 0.001, "l1" = 0, "dropout" = 0.5. MiMeNet used these hyperparameters to determine the network architecture of each dataset and then trained multiple network models using 10 iterations of 10-fold cross-validation (–num_run_cv 10). The predictive performance of each model was measured by the averaged Spearman correlation coefficients (SCCs) between the predicted and the observed gene expression levels across the samples in testing sets. MiMeNet then generated a background distribution of SCCs through 10 iterations (–num_background 10) of shuffling the dataset and performing a cross-validated evaluation on the shuffled set. This background distribution of SCCs was used to determine a significance cutoff for well-predicted genes. This analysis identified N = 1,214 well-predicted genes and N = 346 GM functional pathways with at least one significant attribution score with a well-predicted gene. MiMeNet then constructed a score matrix of pathway-gene feature attributions between the significant GM functional pathways and well-predicted genes. Finally, MiMeNet clustered the score matrix into N = 8 GM functional pathway modules and N = 7 gene expression modules by finding the

largest number of clusters (within each data type) that improved the area under the cumulative distribution curve (CDF) by > 0.025 (57).

To identify the GM functional pathways most associated with donor species effects on mouse brain gene expression, we first tested each MiMeNet gene expression modules (N = 7) for enrichment of genes that are upregulated in HIMs > MIMs (FDR < 0.2) using Fisher's exact tests (*fisher.test* function in the R package *stats*). Four modules (0, 1, 3, and 6) showed significant enrichments (ORs > 1 and $p_{adj} < 0.05$). We then calculated the mean feature attribution scores between each MiMeNet gene expression module (N = 7) and each MiMeNet GM functional pathway module (N = 8) (by averaging all pathway-gene scores in the given pathway-gene cluster combination). For each MiMeNet GM functional pathway module, we averaged these mean scores across gene clusters 0, 1, 3, and 6 (see above) to identify the MiMeNet GM functional pathway clusters with the highest feature attribution scores across the differential expression enriched gene expression modules (0, 1, 3, and 6).

Data, Materials, and Software Availability. Raw and processed mouse brain gene expression data have been deposited at GEO GSE312570 (33). GM sequences have been deposited at Sequence Read Archive (PRJNA1003977) (80). All code used in this manuscript is available at https://github.com/ardecasien/mouse-gut-brain (34). All code used to analyze the GM data is available at https://github.com/Mallott-Lab/PrimateMicrobiomeandBrainGrowth (58).

ACKNOWLEDGMENTS. KRA is supported as a fellow in CIFAR's Humans and the Microbiome Program. A.R.D. was supported by an NYU MacCracken Fellowship and is currently supported by the Intramural Research Program of the National Institute on Aging.

Author affiliations: [a]Computational and Evolutionary Neurogenomics Unit, National Institute on Aging, Bethesda, MD 20892; [b]Section on Developmental Neurogenomics, National Institute of Mental Health, Bethesda, MD 20892; [c]Department of Anthropology, New York University, New York, NY 10003; [d]New York Consortium in Evolutionary Primatology, New York, NY 10024; [e]Center for Evolution and Medicine, Arizona State University, Tempe, AZ 85281; [f]Department of Anthropology, Northwestern University, Evanston, IL 60208; [g]Department of Biology, Washington University in St. Louis, St. Louis, MO 63130; [h]Department of Biological Sciences, University of California at San Diego, San Diego, CA 92093; [i]Department of Comparative Medicine, The University of Texas MD Anderson Cancer Center, Bastrop, TX 78602; [j]Division of Endocrinology, Diabetes, and Metabolism, Department of Medicine, University of Illinois at Chicago, IL 60612; [k]Jesse Brown VA Medical Center, Chicago, IL 60612; [l]Center for Comparative Medicine, Northwestern University, Chicago, IL 60611; [m]Department of Psychology, University of Texas at Austin, Austin, TX 78712; [n]Innovation and Product Development, The Jackson Laboratory, Sacramento, CA 95838; and [o]Department of Human Evolutionary Biology, Harvard University, Cambridge, MA 02138

1. L. C. Aiello, P. Wheeler, The expensive-tissue hypothesis: The brain and the digestive system in human and primate evolution. *Curr. Anthropol.* **36**, 199–221 (1995).
2. aLissa Ventura-Antunes, S. Herculano-Houzel, Energy supply per neuron is constrained by capillary density in the mouse brain. *Front. Integr. Neurosci.* **16**, 760887 (2022).
3. C. W. Kuzawa *et al.*, Metabolic costs and evolutionary implications of human brain development. *Proc. Natl. Acad. Sci.* **111**, 13010–13015 (2014).
4. K. Isler, C. P. van Schaik, The expensive brain: A framework for explaining evolutionary changes in brain size. *J. Hum. Evol.* **57**, 392–400 (2009).
5. H. Pontzer *et al.*, Metabolic acceleration and the evolution of human brain size and life history. *Nature* **533**, 390–392 (2016).
6. E. Magden, K. Mansfield, J. Simmons, C. Abee, "Nonhuman primates" in *Laboratory Animal Medicine* J. Fox *et al.*, Eds. (Academic Press, San Diego, 2015), pp. 771–822.
7. D. A. Raichlen, A. D. Gordon, Relationship between exercise capacity and brain size in mammals. *PLoS One* **6**, e20601 (2011).
8. F. N. Syner, M. Goodman, Differences in the lactic dehydrogenases of primate brains. *Nature* **209**, 426–428 (1966).
9. T. Duka *et al.*, Synaptosomal lactate dehydrogenase isoenzyme composition is shifted toward aerobic forms in primate brain evolution. *Brain Behav. Evol.* **83**, 216–230 (2014).
10. R. Haygood, O. Fedrigo, B. Hanson, K.-D. Yokoyama, G. Wray, Promoter regions of many neural-and nutrition-related genes have experienced positive selection during human evolution. *Nat. Preced.* **39**, 1140–1144 (2007).
11. O. Fedrigo *et al.*, A potential role for glucose transporters in the evolution of human brain size. *Brain. Behav. Evol.* **78**, 315–326 (2011).
12. A. L. Bauernfeind, C. C. Babbitt, Metabolic changes in human brain evolution. *Evol. Anthropol. Issues News Rev.* **29**, 201–211 (2020).
13. C. Huang, X. Yu, W. Liao, The expensive-tissue hypothesis in vertebrates: Gut microbiota effect, a review. *Int. J. Mol. Sci.* **19**, 1792 (2018).
14. S. Sanna *et al.*, Causal relationships among the gut microbiome, short-chain fatty acids and metabolic diseases. *Nat. Genet.* **51**, 600–605 (2019).
15. K. Oliphant, E. Allen-Vercoe, Macronutrient metabolism by the human gut microbiome: Major fermentation by-products and their impact on host health. *Microbiome* **7**, 1–15 (2019).
16. J. Qin *et al.*, A metagenome-wide association study of gut microbiota in type 2 diabetes. *Nature* **490**, 55–60 (2012).
17. V. K. Ridaura *et al.*, Gut microbiota from twins discordant for obesity modulate metabolism in mice. *Science* **341**, 1241214 (2013).
18. A. L. Bauernfeind *et al.*, Aerobic glycolysis in the primate brain: Reconsidering the implications for growth and maintenance. *Brain Struct. Funct.* **219**, 1149–1167 (2014).
19. Y. Ma *et al.*, Fatty acid metabolism and acyl-CoA synthetases in the *liver-gut axis*. *World J. Hepatol.* **13**, 1512–1533 (2021).
20. R. J. Cater *et al.*, Structural basis of omega-3 fatty acid transport across the blood–brain barrier. *Nature* **595**, 315–319 (2021).
21. A. Visconti *et al.*, Interplay between the human gut microbiome and host metabolism. *Nat. Commun.* **10**, 1–10 (2019).
22. F. Bäckhed *et al.*, The gut microbiota as an environmental factor that regulates fat storage. *Proc. Natl. Acad. Sci.* **101**, 15718–15723 (2004).
23. X. Zhang *et al.*, Human gut microbiota changes reveal the progression of glucose intolerance. *PLoS One* **8**, e71108 (2013).
24. E. E. Canfora, J. W. Jocken, E. E. Blaak, Short-chain fatty acids in control of body weight and insulin sensitivity. *Nat. Rev. Endocrinol.* **11**, 577–591 (2015).
25. A. M. Cheney *et al.*, Gut microbiome dysbiosis drives metabolic dysfunction in Familial dysautonomia. *Nat. Commun.* **14**, 218 (2023).
26. H. E. Vuong, E. Y. Hsiao, Emerging roles for the gut microbiome in autism spectrum disorder. *Biol. Psychiatry* **81**, 411–423 (2017).
27. J. T. Morton *et al.*, Multi-level analysis of the gut–brain axis shows autism spectrum disorder-associated molecular and microbial profiles. *Nat. Neurosci.* **26**, 1208–1217 (2023).
28. K. R. Amato *et al.*, Convergence of human and old world monkey gut microbiomes demonstrates the importance of human ecology over phylogeny. *Genome Biol.* **20**, 1–12 (2019).
29. K. R. Amato *et al.*, Evolutionary trends in host physiology outweigh dietary niche in structuring primate gut microbiomes. *ISME J.* **13**, 576–587 (2019).
30. A. Cohen, *Following the Gut: A Measurable Connection between the Gut Microbiome and Brain Size* (University of Colorado at Boulder, 2021).
31. S. R. Leigh, Brain growth, life history, and cognition in primate and human evolution. *Am. J. Primatol. Off. J. Am. Soc. Primatol.* **62**, 139–164 (2004).
32. E. K. Mallott *et al.*, The primate gut microbiota contributes to interspecific differences in host metabolism. *Microb. Genomics* **10**, 001322 (2024).
33. A. R. DeCasien *et al.*, GSE312570. Gene Expression Omnibus. https://www.ncbi.nlm.nih.gov/geo/query/acc.cgi?acc=GSE312570. Deposited 4 December 2025.
34. A. R. DeCasien *et al.*, ardecasien/mouse-gut-brain. GitHub. https://github.com/ardecasien/mouse-gut-brain. Deposited 15 July 2025.
35. Y. Zhu *et al.*, Spatiotemporal transcriptomic divergence across human and macaque brain development. *Science* **362**, eaat8077 (2018).
36. H. J. Kang *et al.*, Spatio-temporal transcriptome of the human brain. *Nature* **478**, 483–489 (2011).
37. A. T. McKenzie *et al.*, Brain cell type specific gene expression and co-expression network architectures. *Sci. Rep.* **8**, 1–19 (2018).
38. C. A. Hunt, L. J. Schenker, M. B. Kennedy, PSD-95 is associated with the postsynaptic density and not with the presynaptic membrane at forebrain synapses. *J. Neurosci.* **16**, 1380–1388 (1996).
39. X. Liu *et al.*, Extension of cortical synaptic development distinguishes humans from chimpanzees and macaques. *Genome Res.* **22**, 611–622 (2012).
40. X. Liu *et al.*, Disruption of an evolutionarily novel synaptic expression pattern in autism. *PLoS Biol.* **14**, e1002558 (2016).
41. G. Muntané *et al.*, Interhemispheric gene expression differences in the cerebral cortex of humans and macaque monkeys. *Brain Struct. Funct.* **222**, 3241–3254 (2017).
42. K. M. Harris, J. K. Stevens, Dendritic spines of CA 1 pyramidal cells in the rat hippocampus: Serial electron microscopy with reference to their biophysical characteristics. *J. Neurosci.* **9**, 2982–2997 (1989).
43. G. N. Elston *et al.*, Specializations of the granular prefrontal cortex of primates: Implications for cognitive processing. *Anat. Rec. A Discov. Mol. Cell. Evol. Biol.* **288A**, 26–35 (2006).
44. C. C. Sherwood *et al.*, Invariant synapse density and neuronal connectivity scaling in primate neocortical evolution. *Cereb. Cortex.* **30**, 5604–5615 (2020).
45. R. Benavides-Piccione, I. Ballesteros-Yáñez, J. DeFelipe, R. Yuste, Cortical area and species differences in dendritic spine morphology. *J. Neurocytol.* **31**, 337–346 (2002).
46. A. A. Galakhova *et al.*, Evolution of cortical neurons supporting human cognition. *Trends Cogn. Sci.* **26**, 909–922 (2022).
47. P. Lennie, The cost of cortical computation. *Curr. Biol.* **13**, 493–497 (2003).
48. E. Masliah, R. D. Terry, M. Alford, R. DeTeresa, Quantitative immunohistochemistry of synaptophysin in human neocortex: An alternative method to estimate density of presynaptic terminals in paraffin sections. *J. Histochem. Cytochem.* **38**, 837–844 (1990).
49. G. Dumas, S. Malesys, T. Bourgeron, Systematic detection of brain protein-coding genes under positive selection during primate evolution and their roles in cognition. *Genome Res.* **31**, 484–496 (2021).
50. W. G. Pembroke, C. L. Hartl, D. H. Geschwind, Evolutionary conservation and divergence of the human brain transcriptome. *Genome Biol.* **22**, 52 (2021).
51. P. Khaitovich, Parallel patterns of evolution in the genomes and transcriptomes of humans and chimpanzees. *Science* **309**, 1850–1854 (2005).
52. S. Berto *et al.*, Accelerated evolution of oligodendrocytes in the human brain. *Proc. Natl. Acad. Sci.* **116**, 24334–24342 (2019).
53. K. Bonnycastle, E. C. Davenport, M. A. Cousin, Presynaptic dysfunction in neurodevelopmental disorders: Insights from the synaptic vesicle life cycle. *J. Neurochem.* **157**, 179–207 (2021).
54. L. Carroll *et al.*, Autism spectrum disorders: Multiple routes to, and multiple consequences of, abnormal synaptic function and connectivity. *Neuroscientist* **27**, 10–29 (2021).
55. J. Hill *et al.*, Similar patterns of cortical expansion during human development and evolution. *Proc. Natl. Acad. Sci.* **107**, 13135–13140 (2010).
56. M. Pourmajidian, J. Y. Hansen, G. Shafiei, B. Misic, A. Dagher, Mapping energy metabolism systems in the human brain. bioXriv [Preprint] (2025), 10.1101/2025.03.17.643763 (Accessed 20 May 2025).

57. D. Reiman, B. T. Layden, Y. Dai, MiMeNet: Exploring microbiome-metabolome relationships using neural networks. *PLoS Comput. Biol.* **17**, e1009021 (2021).
58. E. K. Mallot, *et al.*, Mallott-Lab/PrimateMicrobiomeandBrainGrowth. Github. https://github.com/Mallott-Lab/PrimateMicrobiomeandBrainGrowth. Deposited 19 July 2023.
59. M. Laubach, L. M. Amarante, K. Swanson, S. R. White, If anything what, is rodent prefrontal cortex? *eNeuro* **5**, ENEURO.0315-18.2018 (2018).
60. G. Paxinos, K. B. Franklin, Thyrotropin-releasing hormone receptor binding sites: autoradiographic distribution in the rat and guinea pig brain. *J. Neurochem.* **45**, 1448–1463 (2004).
61. E. S. Lein *et al.*, Genome-wide atlas of gene expression in the adult mouse brain. *Nature* **445**, 168–176 (2007).
62. M. Martin, Cutadapt removes adapter sequences from high-throughput sequencing reads. *EMBnet. journal* **17**, 10 (2011).
63. B. Langmead, C. Wilks, V. Antonescu, R. Charles, Scaling read aligners to hundreds of threads on general-purpose processors. *Bioinformatics* **35**, 421–432 (2019).
64. R. C. Team, R: A language and environment for statistical computing (2013).
65. M. D. Robinson, D. J. McCarthy, G. K. Smyth, edgeR: A Bioconductor package for differential expression analysis of digital gene expression data. *Bioinformatics* **26**, 139–140 (2010).
66. M. E. Ritchie *et al.*, Limma powers differential expression analyses for RNA-sequencing and microarray studies. *Nucleic Acids Res.* **43**, e47 (2015).
67. G. E. Hoffman, E. E. Schadt, Variancepartition: Interpreting drivers of variation in complex gene expression studies. *BMC Bioinformatics* **17**, 483 (2016).
68. G. E. Hoffman, Theory and Practice of random effects and REML in variance Partition and dream (2020).
69. Y. Benjamini, Y. Hochberg, Controlling the false discovery rate: A practical and powerful approach to multiple testing. *J. R. Stat. Soc. Ser. B. Methodol.* **57**, 289–300 (1995).
70. K. L. Chiou *et al.*, Multiregion transcriptomic profiling of the primate brain reveals signatures of aging and the social environment. *Nat. Neurosci.* **25**, 1714–1723 (2022).
71. P. Charruau *et al.*, Pervasive effects of aging on gene expression in wild wolves. *Mol. Biol. Evol.* **33**, 1967–1978 (2016).
72. K. L. Chiou *et al.*, Genomic signatures of high-altitude adaptation and chromosomal polymorphism in geladas. *Nat. Ecol. Evol.* **6**, 630–643 (2022).
73. S. Durinck *et al.*, BioMart and Bioconductor: A powerful link between biological databases and microarray data analysis. *Bioinformatics* **21**, 3439–3440 (2005).
74. J. Rtsne. Krijthe, T-distributed stochastic neighbor embedding using a Barnes-Hut implementation. Version 0.15 (2015).
75. T. Konopka, umap: Uniform Manifold Approximation and Projection. R package version 0.2. 5.0 (2020).
76. G. Yu, clusterProfiler: A universal enrichment tool for functional and comparative study. http://biorxiv.org/lookup/doi/10.1101/256784 (2018), 10.1101/256784.
77. S. Pletscher-Frankild, A. Pallejà, K. Tsafou, J. X. Binder, L. J. Jensen, Diseases: Text mining and data integration of disease–gene associations. *Methods* **74**, 83–89 (2015).
78. M. F. Glasser *et al.*, A multi-modal parcellation of human cerebral cortex. *Nature* **536**, 171–178 (2016).
79. F. Váša *et al.*, Adolescent tuning of association cortex in human structural brain networks. *Cereb. Cortex.* **28**, 281–294 (2018).
80. E. K. Mallot *et al.*, "Influences of the primate gut microbiota on mouse metabolism". Sequence Read Archive. https://www.ncbi.nlm.nih.gov/bioproject?term=PRJNA1003977. Deposited 9 August 2023.
81. E. A. Franzosa *et al.*, Species-level functional profiling of metagenomes and metatranscriptomes. *Nat. Methods* **15**, 962–968 (2018).